The wild west of the Orion nebula

Alba Fernández-Martín ,[1][*] William J. Henney,[1] M. Teresa García-Díaz[2]
and S. Jane Arthur[1]

[1]*Instituto de Radioastronomía y Astrofísica, UNAM, Apartado Postal 3-72, 58090 Morelia, Michoacán, México*
[2]*Instituto de Astronomía, UNAM, Km 103 Carretera Tijuana-Ensenada, 22860 Ensenada, Baja California, México*

ABSTRACT

Key words: keyword1 – keyword2 – keyword3 – keyword4 – keyword5 – keyword6

1 INTRODUCTION

2 OBSERVATIONS AND DATA REDUCTION

2.1 Observations

High-resolution spectroscopic observations were obtained at the 2.1-m telescope of the Observatorio Astronómico Nacional San Pedro Mártir (Baja California, México) in a f/7.5 configuration using the MES-SPM instrument (Manchester Echelle Spectrometer; Meaburn et al. 2003). A total of 62 spectra were obtained from seven sets of observations carried out in 2006, 2007, 2010, 2013 and 2015. The number of positions acquired in each set of observations, dates, exposition times and airmass during the observations are summarized in Table 1.

For the 2006, 2007a, 2007b and 2010 observations the instrument was equipped with the detector SITE-3 CCD, which is an array of 1024×1024 (24μm) pixels giving a spatial resolution of 0.321 arcsec/pix (without considering the binning). On the other hand, the CDD for the 2013a, 2013b and 2015 sets, Marconi-2, was a detector with 2048×2048 square pixel, each 13.5 μm, giving a spatial resolution of 0.176 arcsec/pix (without considering the binning). The slit width was set at 150μ (1.95 arcsec on the sky) throughout the observation and it was oriented in the north-south direction for 2006, 2007a, 2007b and 2010 observations and in the east-west direction for the 2013a, 2013b and 2015 ones.

In order to establish the exact position of the slit in each pointing we took direct slit images of short duration, in which the diffraction grating was replaced by a mirror. Additionally, thorium-argon lamp spectra were taken for wavelength calibration between each slit position.

Finally, taking the seven data sets into account, we get 56 slit-positions in Hα, [N II]λ6548 and [N II]λ6584, lines spanning an interval of 217 arcmin in RA and 9 arcmin in DEC. In addition, exposures in [S II]λ6717 and [S II]λ6730

were also observed in four pointings and [O III]λ5007 in two positions, as indicated in Table 1. In order to illustrate the spatial distribution of the observations in Fig. 1 we show the 56 slit positions observed in Hα+[N II] plotted over an Hα image obtained from Da Rio et al. (2009).

2.2 Data reduction

The spectra were reduced using IRAF[1] by following the standard procedure for 2D spectroscopic observations (bias subtraction, flat-fielding and cosmic ray removal). The wavelength calibration was performed using thorium-argon arcs taken between each slit position.

After transforming all the spectra to a common heliocentric velocity frame, we performed a series of further corrections to obtained well calibrated spectra in a self-consistent way.

(i) An astrometric solution was found for each of the spectra using nearby stars. This allowed us to accurately determine the slit position of each exposure.

(ii) In order to compensate the variations in the sky transparency and seeing between exposures we compare our spectra with a deep Hα image of the region obtained from Da Rio et al. (2009) with the Wide Field Imager (WFI) at the 2.2-m MPG/ESO telescope at La Silla. This was done by fitting a low-order Chebyshev polynomial to the spectra to WFI profile ratio. With this we obtained a brightness normalization factor for each spectra, as well as a correction for flux gradients along the slits. The corrections are typically lower than 15 percent. This comparison also allowed us to flux-calibrate

---

[*] E-mail: a.fernandez@crya.unam.mx

[1] The Image Reduction and Analysis Facility IRAF is distributed by the National Optical Astronomy Observatories, which are operated by Association of Universities for Research in Astronomy, Inc., under cooperative agreement with the National Science Foundation.

Table 1. Summary of the data set observed with the spectrograph MES-SPM.

Set name	Dates	# Slits[a]	Orientation	Spatial resolution[b] (arcsec pix^{-1})	Cover area (arcmin^2)	Exp. time[c] (s)	Airmass[d]
2006	2006 Feb 5	11/0/0	north-south	0.624	6×6	300(3)/600(8)	1.68
2007a	2007 Jan 10	3/1/1	north-south	0.624	2×6	600	1.67
2007b	2007 Jan 13	7/0/0	north-south	0.624	14×6	600	1.30
2010	2010 Jan 15,16,17	17/3/1	north-south	0.624	17×6	450(1)/600(20)	1.37
2013a	2013 Feb 16,18,19	11/0/0	east-west	0.527	100×2	450(1)/600(10)	1.52
2013b	2013 Dec 11	5/0/0	east-west	0.527	114×0.2	600	1.49
2015	2015 Feb 3	2/0/0	east-west	0.351	88×0.2	600	1.29

[a] Number of slit positions observed in Hα+[N ii]$\lambda\lambda$6548,6584 / [S ii]$\lambda\lambda$6717,6731 / [O iii]λ5007.

[b] Final spatial resolution taking the spatial binning into account.

[c] 2006, 2010 and 2013a spectra were taken with different exposure times (separated by a bar). Number of position acquired with each exposure time are indicated in brackets. This was taking into account when combining images in the data reduction.

[d] Mean value during the observations.
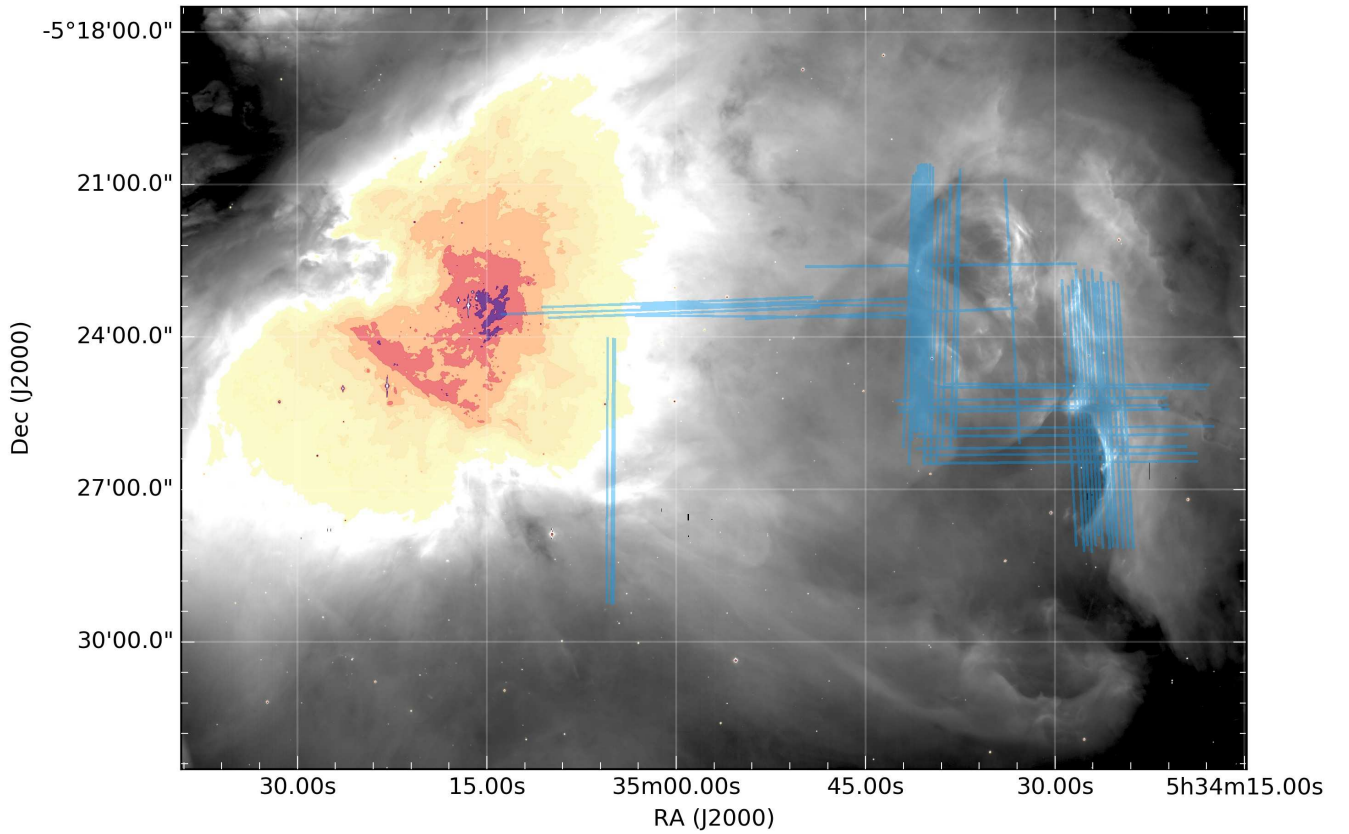
Figure 1. Positions and orientations of the spectroscopic settings observed in Hα+[N ii] with MES-SPM (in blue) plotted over the Hα image of the western region of the Orion nebula obtained from Da Rio et al. (2009). North is up and east to the left.

our spectra, using the spectrophotometry provided by Weilbacher et al. (2015) with MUSE in common regions. Figure 2 shows a three-panel plot with the flux calibration for one of the positions.

(iii) Continuum emission was removed by fitting a two-dimensional Chebyshev function. For each exposure a background section was selected including only line-free regions of the spectrum (we use an excluded velocity window of -10 to +40 km s^{-1} in heliocentric velocity around the line core).

In addition we use an intensity threshold to distinguish high-velocity knots from noise.

Figure 3 shows the resultant calibrated two-dimensional spectra in Hα (top row) and [N ii] (bottom row) for three representative slit positions.
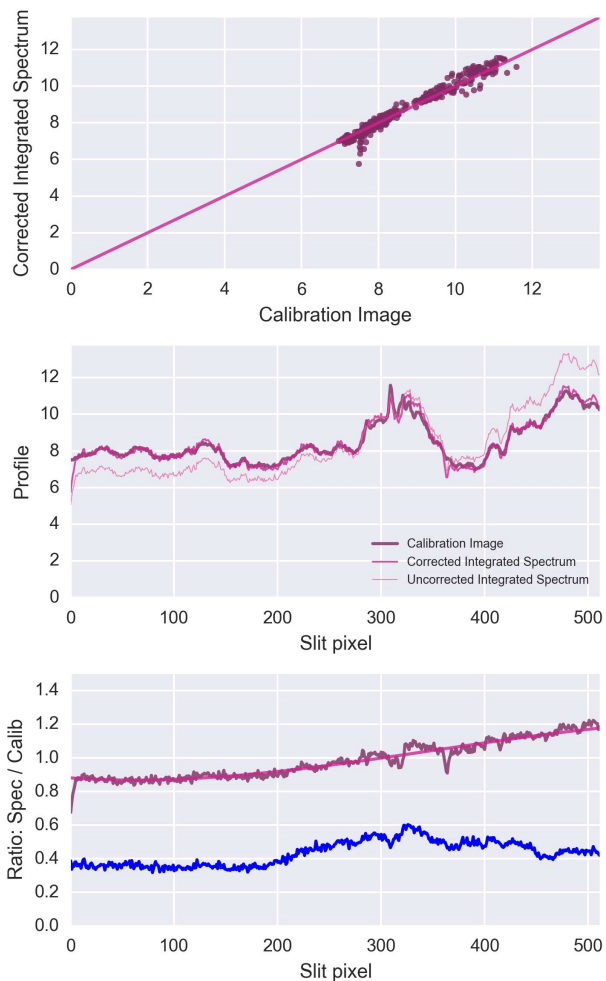
Figure 3. Calibrated two-dimensional spectra for three representative slit positions. The top row shows the Hα emission line and the bottom one the [N II]$\lambda6584$ emission line.

Figure 2. Example of flux-calibration of one of the 2006 spectra in Hα. Top panel: calibrated spectrum profile plotted against calibration WFI image profile. Centre panel: corrected, uncorrected and calibration WFI spectra profiles along the slit. Bottom panel: Chebyshev polynomial function used for calibration (purple), spectrum-WFI ratio corrected (pink) and uncorrected (blue) plotted along the slit.

2.3 Isovelocity maps

In order to better reveal the spatio-kinematical patterns in the observed region, the slit spectra were combined and interpolated to produce isovelocity channel maps. To that end, we carried out the following steps.

First, we built an orthogonal RA-DEC grid placing all the slits onto there by looping over slit profiles extracted in a given wavelength (heliocentric velocity) window. On those grid pixels in which two or more slits fall, the intensity was estimated as the mean weighted by the slit quality. Grid pixels where no slit falls were left transparent.

Due to observational differences between each set of observations (i.e. spatial resolution and seeing) we generated multi-resolution maps in order to not degrade the quality of the better spectra. To do that, we build several isovelocity maps onto grids with binning of 2 (better resolution), 4, 8, 16 and 32 (worst resolution).
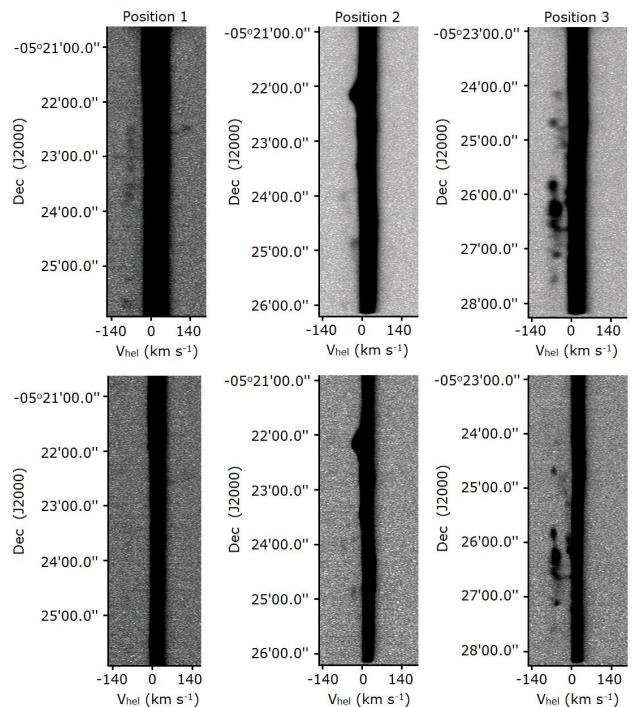
Finally, all the grids were combined to obtain multigrid smoothed channel maps with a spatial resolution ranging from 0.5 to 15.1 arcsec pix^{-1}. We created maps in several velocity ranges to find kinematical structures at different velocities: the narrow band channels cover velocities from -10 to -110 km s^{-1} and from +10 to +170 km s^{-1} in steps of 20 km s^{-1}, while the wide bands span from +0 to +60, -60 to +0 and -120 to -60 km s^{-1}. The line core is also sampled in the channel ranging from -10 to +10 km s^{-1}. These isovelocity maps were performed only in Hα and [N II] emission lines, because in [S II] and [O III] the spatial coverage of the observations is too small.

A particularly useful method of identifying large-scale velocity systems is to study images that are color-coded to simultaneously show different velocity ranges. In Fig. 4 we present combined isovelocity channel maps for [N II] covering the heliocentric velocity range from -10 to +50 km s^{-1}. The analysis of the isovelocity channel maps reveal a rich harvest of results that can be subdivided into several distinct topics. In the following two sections we provide an empirical description of the kinematical features observed by using the isovelocity channel maps and the position-velocity spectra. First we describe major features seen in the western outskirts of the Orion nebula. Later we focus on blue and redshifted knots with high radial velocity.
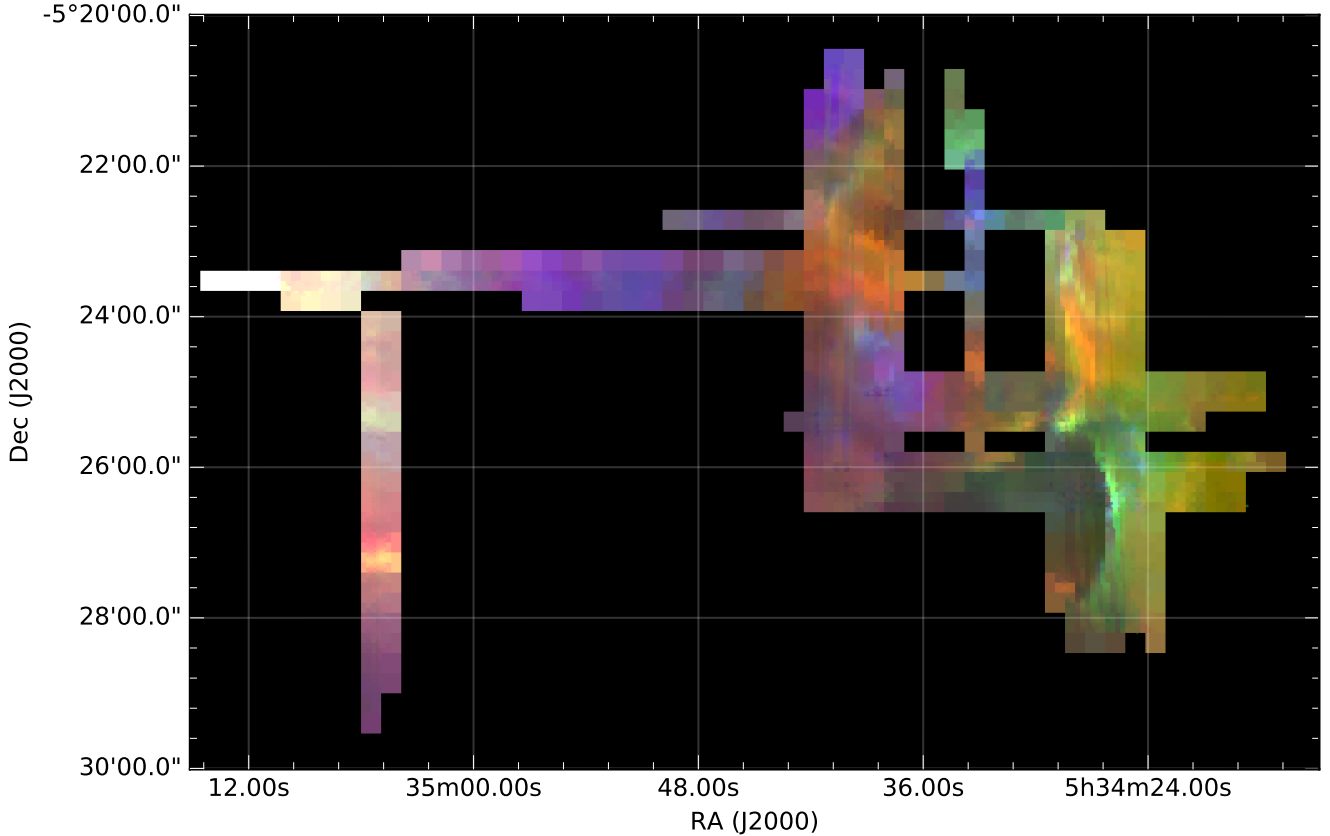
Figure 4. RGB composite image of the western region of the Orion nebula obtained from the [N II] isovelocity maps. Red corresponds to the channel maps with heliocentric velocity between +30 and +50 km s^{-1}, green between +10 and +30 km s^{-1} and blue between -10 and +10 km s^{-1}. North is up and east to the left.

Figure 5. WILL/YO: Mapa RGB en el rango rojo con estructuras a gran escala identificadas (los 4 red bow-shocks descritos)

3   LARGE-SCALE STRUCTURES

At least four bow-shocks lie in the western part of our observation FoV. These features show velocities slightly redshifted with respect to the systematic velocity of the nebula and their appearance is detected in both Hα and [N II] isovelocity maps. The bow-shocks identified are illustrated in Fig. 5. To describe their location we use their positions relative to the feature we will call the Western Wall (WW). **(WILL: describir Western Wall)**. In addition, in order to confirm the identification and make precise locations of the structures we resort to high spatial resolution images obtained from Da Rio et al. (2009) with the WFI (described above), Bally et al. (2006) with the Advanced Camera for Surveys (ACS) of the Hubble Space Telescope and Robberto et al. (2013) also with the ACS (hereinafter D09, B06 and R13).

The largest of the four bow-shocks is located on the northeast side of the WW (we identified it as NE red-bow shock). It crosses LL2, but is oriented in its opposite direction, towards the west part of the nebula. The channel maps reveal that it is moving with velocities from +0 to +50 km s^{-1} in both Hα and [N II], although some regions show velocities up to 90 km s^{-1} in Hα. The morphology of this bow is very well defined in the high-spatial resolution images from D09, B06 and R13, especially in B06 where it seems to be a region composed of various shocks moving toward the west.

The brighter, west-facing bow-shock we identify is located beyond the northwest of the WW (called NW red bow-shock) and it seems to mimic the orientation of the northeast one. The bow-shock is well defined in Hα, detected at velocities from +10 to +70 km s^{-1}, but is not clear in the [N II] maps, in which there are extended emission at the north of the bow-shock moving in the same range of velocities. Attending to the images, this region is spatially coincident only with the observations of D09 and R13, where it can be identified with the brighter emission of the bow-shock. However, this feature shows a less well defined bow shape than the others, as if only the edge of the paraboloid were detected. This may be because it is located close to the boundary of the WW, where the S/N is lower, preventing the detection the whole bow-shock.

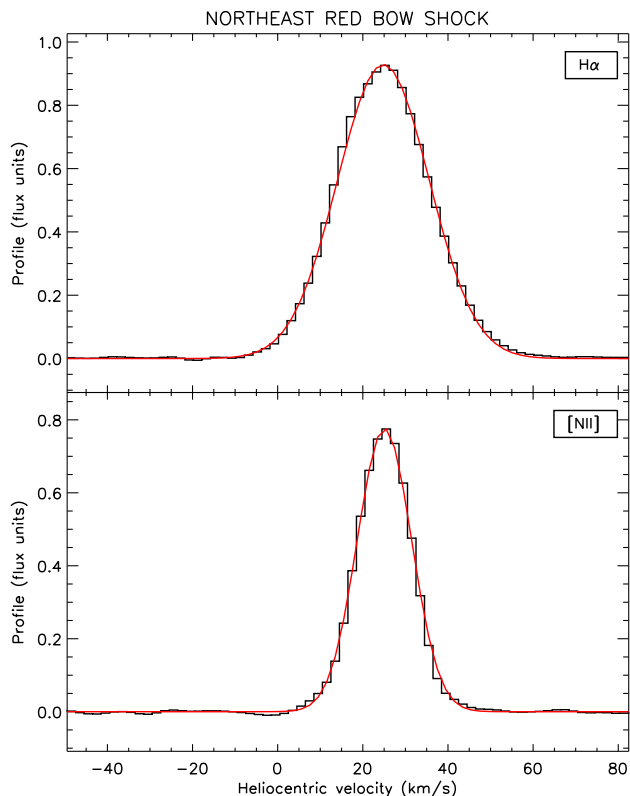On the western side of the WW we identified the third

Figure 6. Spectral profiles in Hα (top) and [N II] (bottom) along the line of sight of the red bow-shock located to the northeast of the WW. The black line represents the profile extracted from the slit spectra after the core subtraction. The red line indicates the Gaussian fit performed.

red bow-shock (called SW). The composite channel maps show that it is not so redshifted as the other two presented above, moving with velocities from +10 to +50 km s^{-1} in Hα and [N II]. The bow-shock structure is clearly identifiable in the images obtained from D09 and R13 and it extends toward the southwest part of the Orion nebula. Analysing the Hα images we observed that in this bow-shock it can be distinguished two orientations: the first one moving to the west (SW-W) and the second one moving to the southwest (SW-S). To check this, the kinematical study of the SW shock will be performed differentiating the two possible sub-shocks.

Finally, the isovelocity maps reveal a red bow-shock located to the southeast that is dimmer than the other features described (identified as SE). It is detected in Hα and [N II] maps with velocities ranging from +10 to +50 km s^{-1} and it crosses LL3. The structure of this bow-shock is not totally detected in the isovelocity maps because the slit positions observed do not spread enough in the southern part. Nonetheless, the whole bow morphology is perfectly identified in the Hα images from D09, B06 and R13.

To estimate the velocity of the shocks we selected those slit positions which cross the bow-shocks in representative regions, if possible in areas close to the head of the bow. We found that no slit positions observed in [S II] or [O III] are

Table 2. Properties of the red bow-shocks detected in the western region of the Orion nebula.

Bow-shock	V_{hel} (km s^{-1})		FWHM (km s^{-1})		Flux (Flux units)	
	Hα	[N II]	Hα	[N II]	Hα	[N II]
NE	23.8	24.1	25.4	15.0	12.6±0.4	6.2±0.2
NW†	25.0	25.0	27.8	12.3	9.4±1.6	3.1±0.8
SE	21.9	20.6	23.9	15.7	5.0±0.3	2.3±0.2
SW-S	24.0	22.5	23.3	14.1	2.8±0.3	1.5±0.2
SW-W	21.5	20.9	25.7	17.2	13.4±0.6	9.1±0.3

† Bad subtraction of the line core.

located near the bow-shocks, so we performed this study only in Hα and [N II] emission lines. One-dimensional spectra were extracted in the position of the shocks with an aperture of nine pixels. The thermal Doppler broadening of the line core (more relevant in Hα than in [N II]) avoids to identify the profile of the shocks (with velocities around +20 km s^{-1}). For this reason, a subtraction of the line core was performed as a background. For each slit position we extracted one-dimensional spectra in two representative regions which were combined by a mean to sample the background variations. These regions were selected as close to perpendicular to shock as possible and in areas outside the bow-shocks to avoid that the emission of the shocked gas dominates the spectrum. Once the line core was subtracted to all the one-dimensional spectra we performed Gaussian fits to the shock profiles weighted by the uncertainties of the background. Figure 6 shows the spectral profile of one of the red bow-shocks (the northeast one) with the core subtraction and the Gaussian fit performed. All the fit performed worked well except for the NW shock where the background profile includes blueshifted emission near the line core making impossible to make a good subtraction on the blue side of the line.

Table 2 lists the properties measured for the four red bow-shocks in Hα and [N II]. Each studied shock is identified in the first column. The second and third columns give the heliocentric velocities measured for the centre of the Gaussian fits. Full width at half maximum (FWHM) are presented in columns 4 and 5, while fluxes obtained from the fits are shown in columns 6 and 7. The statistical errors associated with the measured fluxes were calculated integrating the residue of the fit over the whole velocity range of the line.

4 HIGH-VELOCITY KNOTS

Analysing the position-velocity spectra and the isovelocity maps we detect five redshifted features at high-velocities located nearby to LL1 and LL2. All of them are already catalogued by Henney et al. (2013) and we do not perform any study of them in this work. On the other hand, we find 50 high-velocity blueshifted features in the isovelocity maps. They are distributed over the whole observation FoV, although, as can be appreciated in Fig. 7, there is a concentration of blueshifted knots to the south-west.
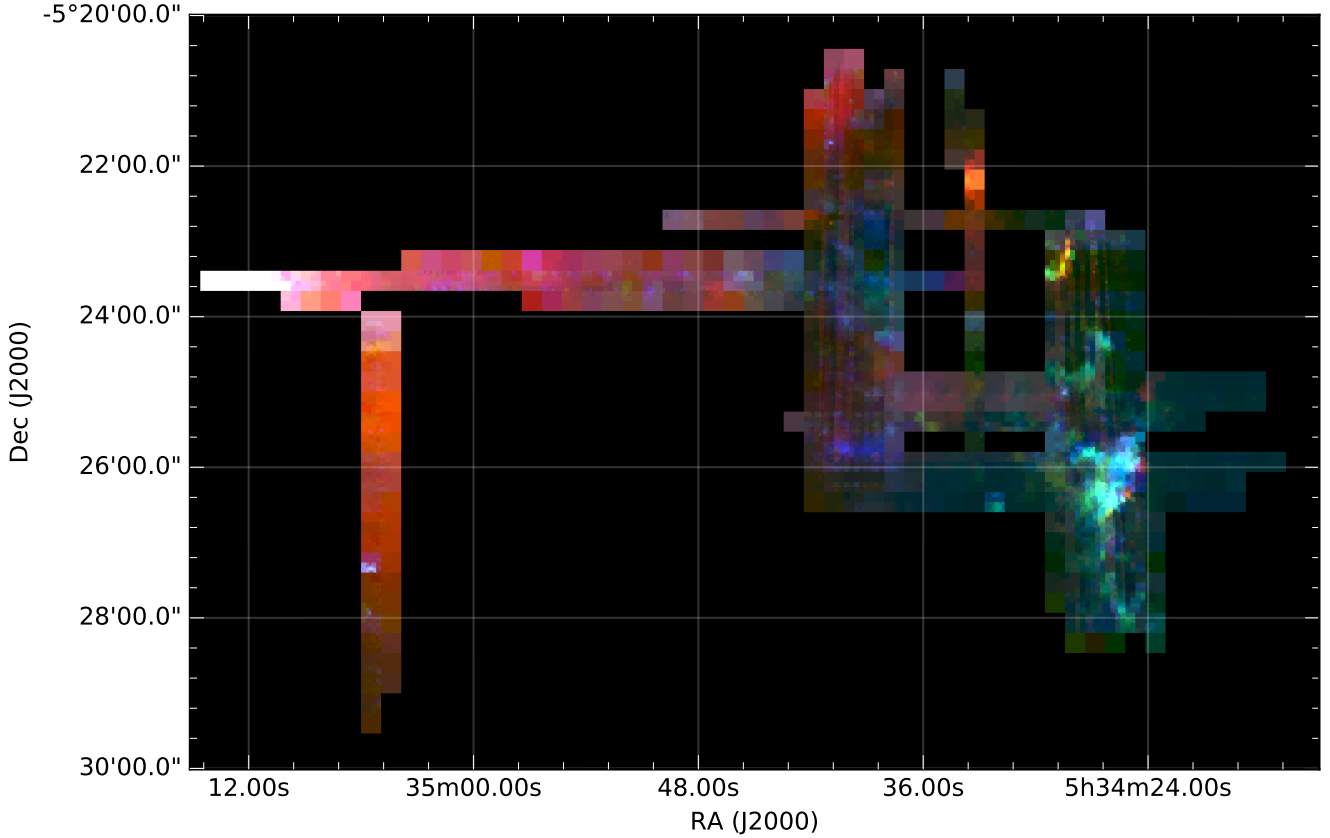
Figure 7. WILL/YO: mapa RGB en azul + finding chart con knots identificados

In order to obtain the kinematical properties of the blue knots we resorted to the 2D spectra. First, taking the spatial position into account, the knots were identified in the spectra. For those cases in which a knot was sampled by several slit positions (in the same emission line), we chose the spectra with better S/N and resolution (i.e. well resolved knots). Then, the one-dimensional spectra were extracted for each knot with an aperture optimized for covering the spatial distribution of the knot minimizing the contamination of adjacent pixels. The extraction was performed with the same aperture for all the emission lines taking the spatial scales differences into account.

To study the one-dimensional profiles we performed Gaussian fits to the line core and the high-velocity component by using our own routines. In the line core we performed a deconvolution into multiple Gaussian components to sample both systematic velocity due to the emission from the ionized layer of the nebula and the light scattered by dust in the photon-dominated region. In the case of the blue knots, their study depends on their velocity: high-blueshifted components were fitted individually by a Gaussian function while for low-blueshifted features the fit was performed simultaneously with the line core. The uncertainties associated with the flux were estimated integrating the residue of the fit. This error points out if the approximation of consider the emission lines as Gaussian functions is acceptable, but it does not take the systematic errors from the calibration into

account. Figure 8 shows an example of the fits performed in Hα and [N II].

This procedure was carried out to obtain information, in a first attempt, in all the emission lines. However, even though the selected slits were situated over the knots, we found that in some knots the emission in [N II], [S II] and/or [O III] is too weak and it prevents identification of the features in the profiles. In these cases we consider upper limits to the flux measuring the uncertainty associated with the continuum at the same heliocentric velocity as for the Hα fits. In addition, several detected knots of the sample present shapes far from Gaussian functions, for them we estimated the emission by integrating the flux between two velocity limits and over a fitted local continuum. In these cases, the flux depends critically on the chosen velocity range. For this reason, we perform measurements between three velocity ranges around the emission line, estimating the flux as the average of the three values and the associated error as the average difference between the two extreme values.

Heliocentric velocities, FWHM and fluxes (with their corresponding errors) are presented in Table 3 for every detected blueshifted high-velocity feature in Hα and [N II]. The last column reports the spatial size of each knot in the orientation of the slit selected to obtain the profile. We also indicate the knots in which the flux was not obtained by Gaussian fits (see footnotes in the table). When naming new com-

Table 3. Heliocentric velocities, FWHM, fluxes and spatial sizes for the blueshifted high-velocity knots studied in Hα and [N II].

Knot	V_{hel} (km s^{-1})		FWHM (km s^{-1})		Flux (Flux units)		Size (arcsec)
	Hα	[N II]	Hα	[N II]	Hα	[N II]	
050-422	-38.91	-38.21	27.06	15.99	2.14±0.16	<0.10[a]	4.4
4242-458	-20.90	-22.54	30.59	17.71	4.21±0.42	0.91±0.04	9.8
4244-554	-16.55	-15.23	28.24	21.23	15.85±1.49	8.26±0.27	14.2
4245-742	-61.27	-61.96	32.27	14.96	0.47±0.07	0.13±0.06	3.1
4252-608	-80.10	-82.25	29.17	19.31	0.99±0.10	0.44±0.02	3.7
4252-616	-16.75	-17.62	37.65	30.12	13.83±1.02	7.71±0.79	6.9
4254-551	-68.29	-68.67	26.12	17.48	6.41±0.11	2.25±0.12	8.1
4258-744	-59.53	-62.18	33.56	27.97	2.01±0.17	0.66±0.09	6.9
4260-612	-64.32	-63.24	38.75	34.10	3.59±0.34	1.43±0.26	4.4
4261-352	-48.29	-47.96	22.98	14.99	<0.42[a]	<0.11[a]	14.3
4261-422	-57.81	-57.74	35.09	28.40	1.31±0.11	0.30±0.04	3.1
4261-626	-59.67	-61.19	35.22	26.62	5.05±0.30	2.99±0.22	5.6
4263-460	-31.88	-32.05	32.94	23.53	1.36±0.22	0.27±0.06	5.7
4265-630	-54.69	-55.00	34.06	29.13	10.08±0.74	3.77±0.42	10.6
4266-615	-57.04	-57.68	31.83	23.17	18.44±0.62	6.53±0.44	16.9
4268-414	-42.08	-41.91	37.92	22.98	0.50±0.13	<0.13[a]	3.1
4271-440	-60.68	-64.06	30.20	16.39	1.26±0.24	0.40±0.03	5.6
4272-545	-64.20	-63.92	28.33	19.96	7.31±0.28	2.64±0.27	10.0
4272-622	-54.43	-55.64	31.17	21.42	2.53±0.15	0.84±0.09	6.9
4273-639	-65.21	-64.84	32.94	19.99	0.48±0.05	<0.12[a]	4.4
4273-704	-57.61	-64.84	33.26	21.98	1.40±0.25	<0.31[a]	16.8
4277-539	-77.01	-77.05	28.24	14.41	0.98±0.09	0.23±0.05	4.4
4280-551	-72.92	-76.29	27.42	22.45	0.63±0.06	0.21±0.02	3.7
4284-308	-36.73	-39.87	28.24	20.12	3.42±0.44	1.65±0.13	5.6
4285-444	-60.15	-59.97	25.87	22.01	0.59±0.08	0.12±0.04	4.4
4289-524	-71.51	-73.52	25.16	17.25	0.82±0.08	0.25±0.04	4.4
4289-647	-32.43	-28.28	28.24	20.71	0.50±0.17	0.18±0.03	4.4
4292-323	-54.91	-56.00	28.58	23.53	3.30±0.26	2.29±0.19	6.9
4293-557	-41.21	-41.14	32.94	18.83	1.11±0.08	0.24±0.03	4.8
4320-626	-64.73	-65.89	27.27	12.33	1.54±0.10	0.27±0.02	6.9
4331-453	-30.21	-32.39	28.24	18.83	1.63±0.21	0.35±0.08	6.8
4332-401	-71.00	-69.93	15.27	13.83	0.15±0.05	0.07±0.02	3.1
4334-560	-67.06	-72.08	16.64	17.10	0.16±0.04	0.09±0.04	5.6
4335-207†	-19.36	-21.52	27.50	15.61	94.23±1.29	25.53±0.55	23.0
4359-521	-37.34	-38.58	31.18	16.00	1.90±0.32	0.35±0.05	6.9
4374-457	-66.67	-67.16	24.58	14.99	0.19±0.07	<0.03[a]	2.6
4376-329	-79.92	-81.66	26.27	15.68	0.49±0.10	0.13±0.02	4.3
4377-526	-70.96	-71.50	28.24	13.30	0.52±0.06	0.07±0.02	3.7
4378-434	-68.00	-68.44	28.24	16.99	0.22±0.04	<0.03[a]	4.3
4381-411	-67.31	-69.64	30.71	17.17	0.44±0.05	0.05±0.01	3.1
4383-343	-63.12	-65.41	38.22	16.46	0.40±0.08	0.07±0.02	3.1
4385-243	-77.62	-78.31	31.38	18.99	0.33±0.05	<0.03[a]	5.6
4389-327	-63.03	-65.38	44.71	15.99	0.67±0.20	0.15±0.01[b]	6.8
4396-541	-90.00	-91.25	23.59	13.72	0.87±0.12	0.11±0.02	8.1
4402-400	-75.26	-78.97	23.53	13.15	0.54±0.08	0.12±0.03	5.6
4405-349	-78.13	-77.93	20.73	15.99	0.14±0.03	<0.04[a]	4.3
4406-330	-68.93	-69.20	23.53	13.99	0.27±0.05	<0.03[a]	5.6
4407-229	-78.61	-80.39	25.93	11.72	0.19±0.04	0.04±0.01	4.4
4409-243	-67.17	-66.78	22.16	12.99	0.18±0.04	<0.02[a]	5.6
4456-324	-68.95	-71.43	19.23	8.99	0.74±0.20	0.14±0.01[b]	6.8

† Knot blended with the line core. Uncertain identification and fit.

[a] Upper limits fluxes obtained from the uncertainties associated with the continuum.

[b] Knots with shapes no Gaussian. Intensities obtained by measuring fluxes under the line.

pact objects, we have followed the convention established by O'Dell & Wen (1994) that evokes the two-dimensional position on the plane of the sky. The first four digits indicate the position of right ascension and the second three digits

the position in declination (both in J2000 epoch and respect to α=5^{h}3X^m:XX^s.X δ=-5°:2X$'$:XX$''$).

The slit positions acquired in [S II] and [O III] have a spatial coverage smaller than in Hα and [N II], and only a few knots were observed in these emission lines. In
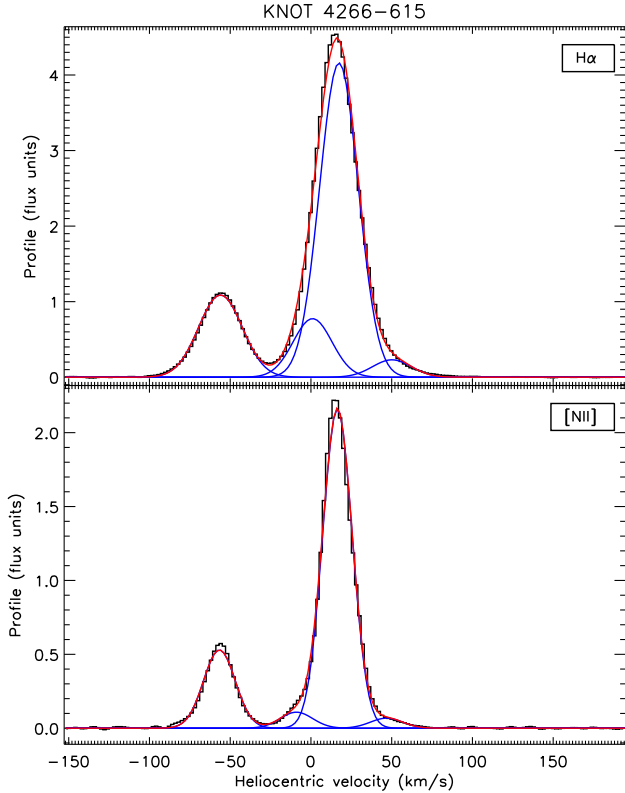
Figure 8. Spectral profile in Hα (top) and [N II] (bottom) along the line of sight of the blue knot 4266-615. The black line represents the original profile extracted from the slit spectra. The velocity components are represented in blue, while the red line indicates the total fit taking all the components into account.

particular, only ten knots were observed in [S II]λλ6717,6731 and eight of them also observed in [O III]λ5007. For this reason, the study in [S II] and [O III] was performed with different aims than for Hα and [N II]; the results of the measurement of the fluxes and the subsequent analysis will be described in the subsection 4.1.

4.1   Physical conditions in blue knots

The slit spectra observed in [S II] and [O III] can be used to estimate the physical conditions in the high-velocity blueshifted knots. To determine the real line intensity emitted by each knot it is important to correct for the effects of foreground dust extinction. With our observations we have not information about the Balmer lines necessary to obtain the extinction coefficient c(Hβ). O'Dell & Harris (2010) (hereinafter OH10) performed long slit observations in the Orion nebula, in particular, four of their slit positions cross the blue knots studied in this section or are located near of them. We decided to adopt their values of c(Hβ) to de-redden our emission lines. In Table 4 we show the association between OH10 slit positions and our knots; in those knots that are close to two slits we consider the average value of both. As can be seen, the extinction coefficient presents values near to zero for all the knots

Table 4. Association between our blueshifted knots and the slit positions observed by O'Dell & Harris (2010). Extinction coeficient and electron temperature presented are the values derived by OH10.

Knot	OH10's slits	c(Hβ)	$T_e([\text{N II}])$ (10^4K)	$T_e([\text{O III}])$ (10^4K)
050-422	11-West	0.26	0.84	0. 78
4254-551	D-North/D-NE	0.005	0.88	0.92
4258-744	D-North	0.01	0.86	0.92
4261-352	D-North	0.01	0.86	0.92
4261-422	D-North	0.01	0.86	0.92
4261-626	D-North/D-NE	0.005	0.88	0.92
4263-460	D-North/27-West	0.01	0.88	0.94
4331-453	27-West	0.01	0.89	0.97
4332-401	27-West	0.01	0.89	0.97
4334-560	D-NE	0.0	0.89	0.92

(except for 050-422), therefore this approximation has an insignificant effect on the corrected fluxes. In table 5 we present the reddening corrected intensities of the emission lines measured for every blue knot relative to Hα. Intensities were derived using the same values of the reddening function f(λ) that OH10. Errors in the emission line ratios were inferred by propagating the observational errors in the fluxes and the reddening constant uncertainties.

The electron density (n_e) was determined from the nebular doublet ratio [S II]λ6717/[S II]λ6731 using the IRAF package TEMDEN based on a five-level statistical equilibrium model (De Robertis et al. 1987; Shaw & Dufour 1995). To estimate n_e, electron temperature (T_e) is requiered, but in this work no emission lines necessary to derive T_e have been observed. Because of it we resorted again to the observations of OH10 to determine T_e from the line intensities of the slits which cross our knots. Although the line intensities that they present in the paper were obtained by integrating the flux over the whole slit, to adopt their values is not a bad approximation because the nebula does not present strong variations in T_e (as can be seen in columns 4 and 5 of Table 4); in addition, the density dependence with the temperature is very small, e.g. variations in T_e from 0.8×10⁴K to 1.2×10⁴K increase n_e less than 100cm⁻³ (which is in the range of the intrinsic uncertainties of the line measurements).

The physical parameters were derived by performing an iterative process for each knot until achieving agreement between the electron density and electron temperature. We used our own measurements of the [S II] line ratio to estimate n_e and OH10 measurements to derive T_e (all the line intensities were de-reddened under the same conditions). The values of n_e inferred for each knot along with their corresponding errors are given in Table 5, as well as $T_e([\text{N II}])$.

It is interesting to emphasise the behaviour of the knot 4261-352. Initially, this knot was not identified because it does not emit in Hα or [N II]. However, when analysing the 2D spectra in [S II] we found a weak, but not negligible, emission in [S II]λ6731 at $V_{hel} \sim$ -48 km s⁻¹, undetected hitherto. Although we estimate the flux of this knot in all the emission
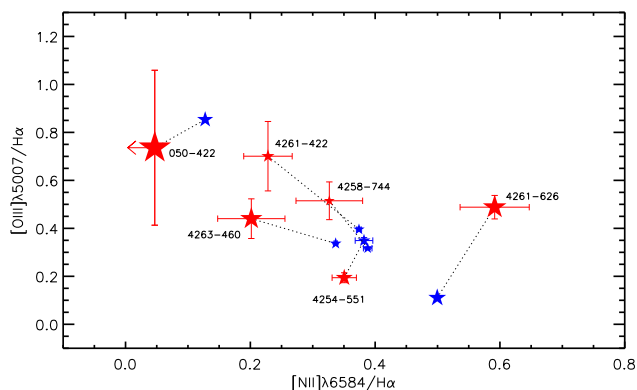
Figure 9. Diagnostic diagram [O III]$\lambda\lambda$5007/Hα versus [N II]$\lambda\lambda$6584/Hα. Red stars represent line intensities derived for the high-velocity blue knots, while those derive for the nebula are represented in blue. Dashed lines connect knots and nebula located at the same region. The symbol sizes are proportional to the electron density.

lines (by integrating the flux in a heliocentric velocity range), only the [S II]λ6731 measurement is reliable, so we can not perform an accurate study of this object. We only can affirm that this is a peculiar object with high electron density (R_{S2} <0.12 implies n_e>10^4cm^{-3}) which does not emit in Hα or [N II]. Maybe it is not associated with the H II region, but it belongs to the the photo-dissociated zone **(WILL: que otro objeto era asi? HH201? referencia?)**.

5 DISCUSSION

The isovelocity maps and the 2D spectra reveal many new features which have been kinematically described in the previous sections. Now, we will interpret these results to **....**

5.1 Discusion red bow-shocks

Pensar que podemos decir, poca informacion.

5.2 Formation of the high-velocity blue knots

In this section, we will discuss how the blue knots described in section 4 relate to the background nebular gas, consider which physical processes are likely to generate the knots and evaluate the role that these processes play in the formation and evolution of the knots. To this end we analyse the results obained for the knots in which the physical properties have been inferred (Table 5). Previously, we explained that the line core was deconvolved into multiple Gaussian functions. When measuring the flux in these components we obtain information about the emission in the nebula in the region of the high-velocities features. To compare the physical conditions in the nebula with the high-velocities knots gives clues about the physical processes involved in the formation of the knots. With this aim, we measure the flux of the line core in the ten spectra associated with the knots observed in [S II] and/or in [O III]. Then, the line ratio relative to Hα were de-reddened and the electron density was derived following

the same procedure as the described before for the knots. The results obtained are presented in Table 5.

The excitation mechanisms of the blue knots can be studied using diagnostic diagrams based on the ratio of strong emission lines: the classic BPT analysis (Baldwin et al. 1981). Using data derived for the nebula and for the knots we generate the diagram [O III]$\lambda\lambda$5007/Hα vs. [N II]$\lambda\lambda$6584/Hα showed in Fig. 9. Line ratios derived for each blue knot are represented by red stars, while blue stars correspond to those measured for the nebula. The derived electron densities are also indicated according with the size of the symbols. Data obtained from the same spectra (i.e. knot and nebula at the same position) are connected by dashed lines.

As can be seen in Table 5, for all the regions studied the blue knots are denser than the nebular gas This observational fact implies that some physical mechanism has compressed the gas when forming the knots. Beside that the increase of density, the gas compression causes a decrease of the ionization parameter. It means that the knots should have more emission in [N II] and less in [O III] than the nebular gas associated in the same region. However, we do not detect this behaviour in any of the knots represented in Fig. 9.

The easier explanation would be to consider the projection effects of the observations: the analysed gas and the knot are located at the same position in the plane of the sky, but they are not spatially coincident in the third dimension. This effect would imply that the three knots which present higher ionization degree than the background gas (4258-744, 4261-422 and 4263-460) are placed insider than the nebular gas studied, closer to the ionizing stars.

Another possible explanation to the behaviour observed in Fig. 9 would be that the detected blue knots had been formed and excited by shocks. In this scenario the shocked gas would suffer two changes with respect to the nebular gas. First, the electron density increases; in particular, a shock with velocities of -70 km s^{-1}(the maximum heliocentric velocity measured in these knots) causes an increase in density of 25 per cent with respect to the nebular gas. This characteristic is observed in all the knots studied.

The second effect caused by a shock is that the temperature increases and the gas is ionized yielding N^{2+} and O^{2+}. Nonetheless, the N^{2+} is an unstable ion and it quickly des-excites to N$^+$, thus in the shocked gas we would expect to observed an increase in the emission of [N II] together with [O III]. This behaviour only is detected in the knot 4261-626. A possible explanation for the knots where we find an increase in [O III] and a decrease in [N II] would be that we were observing a recent shock in which the nitrogen des-excitation has not happened yet (we detect a decrease in [N II] because all the nitrogen is emitting as N^{2+}). To confirm this hypothesis it is necessary to compare our data with shock models. **(WILL: shock models).**

Esto es como un resumen para mi. Completar. Taking these ideas into account, and in the absence of further observation, all we can speculate about the knots are the following conclusions. Attending to the position in the Orion nebula (close the WW) and the increase in [N II], [O III] and

Table 5. Reddening corrected line ratios and physical parameters derived for the blue knots and for the nebula.

Knot	[O III]$\lambda\lambda$5007/Hα		[N II]$\lambda\lambda$6584/Hα		R_{S2}		n_e([S II]) (cm^{-3})		T_e([N II])[a] (10^{4}K)
	Knot	Nebula	Knot	Nebula	Knot	Nebula	Knot	Nebula	
050-422	0.74±0.32	0.853±0.006	<0.05[b]	0.128±0.001	-	1.01±0.04	-	518±74	0.90
4254-551	0.19±0.02	0.349±0.012	0.35±0.02	0.382±0.014	0.98±0.11	1.20±0.07	600±53	229±82	0.88
4258-744	0.51±0.08	0.317±0.006	0.33±0.05	0.388±0.007	>1.41[c]	1.35±0.04	<100	75±37	0.86
4261-422	0.70±0.14	0.395±0.006	0.23±0.04	0.374±0.003	1.19±0.26	1.34±0.03	242±58	86±22	0.86
4261-626	0.49±0.05	0.111±0.003	0.59±0.06	0.500±0.001	0.80±0.07	0.95±0.01	1197±373	668±21	0.88
4263-460	0.44±0.08	0.337±0.003	0.20±0.05	0.337±0.003	>0.83[c]	1.29±0.02	<1078	129±14	0.87
4331-453	-	-	0.22±0.06	0.304±0.004	>0.59[c]	1.27±0.03	<3627	152±27	0.88
4332-401	-	-	0.44±0.20	0.289±0.003	<1.35[c]	1.28±0.05	>100	141±44	0.88
4334-560	-	-	0.57±0.30	0.349±0.004	<0.84[c]	1.30±0.02	>1014	119±21	0.91

[a] Electron temperature derived by adopting the line intensities from OH10. It is the same for the knot and for the nebula.

[b] Upper limit flux obtained from the uncertainties associated with the continuum.

[c] Knots in which one of the [S II] emission line was measured by integrating the flux under the line.

n_e with respect to the background gas, the knot 4261-626 seems to have been excited by a shock. The emission detected in the knots 4261-422, 4263-460 and 4258-744 can be caused by a projection effect (they are closer to the ionising star than the nebular gas) or by a recent shock in which the N^{2+} des-excitation has not happened yet. The decrease in [N II] and [O III] observed in 050-422 and 4254-551 seems indicate some cooling process **(???)**, even though maybe it is also a projection effect which avoids interpreting the observational results.

5.3 Jets and arcs

In this section we relate large-scale structures detected in the nebula (not described before) with the blue knots studied previously. Figure 10 shows the features identified together with the blue knots associated.

Two possible new jets with heliocentric velocities blueshifted with respect to the systematic velocity of the nebula have been found in the isovelocity maps. The first one, called Jet-H, is clearly detected in the velocity range from -110 to -70 km s^{-1} in the Hα and [N II] maps, and it is moving horizontally in the plane of the sky (with $\delta \sim$constant). It is almost sampled by the knot 4396-541 in which we measured a heliocentric velocity of -90 km s^{-1} in Hα and a [N II]/Hα ratio of 0.13. With our observations we cannot provide more information about this jet, however in a forthcoming paper we will present new observations that will allow us to study the proper motions of the Jet-H to disentangle its kinematics and origin.

The second possible jet (Jet-D) is moving diagonally in the plane of the sky and it is detected in the isovelocity maps with velocities between -70 and -30 km s^{-1} in Hα and [N II]. This jet is more difficult to identify in the maps because part of its structure is not covered by our observations. Spatially it is sampled by three of the blue knots studied (from east to west: 4331-453, 4293-557 and 4272-622) in which we measured velocities of -30, -41 and -54 km s^{-1} respectively. Thus, this is a jet moving faster in its head than in its tail, possibly because it is moving

through a medium less and less dense.

On the other hand, when analysing the high spatial resolution images from B06, D09 and R13 we find large-scale structures with high superficial brightness located to the western side of the WW. These arcs are not detected in the isovelocity maps, however we find that in the inner region of each arc there are knots. Thus, these structures are arcs which are strongly emitting in Hα and with blueshifted knots inside. Figure 10 shows the six arcs identified in the Western region of the Orion nebula. **Completar**

- A with 4244-554 V_{hel} ~-16 km s^{-1}
- B with 4252-616 V_{hel} ~-16 km s^{-1}
- C no knot (4260-612?)
- D with 4261-626 V_{hel} ~-59 km s^{-1} and n_e=1000cm^{-3}
- E with 4266-615 with V_{hel} ~-57 km s^{-1}
- F no knot (4273-639, 4273-704?)

6 CONCLUSIONS

ACKNOWLEDGEMENTS

REFERENCES

Baldwin, J. A., Phillips, M. M., & Terlevich, R. 1981, PASP, 93, 5

Bally, J., Licht, D., Smith, N., & Walawender, J. 2006, AJ, 131, 473

Da Rio, N., Robberto, M., Soderblom, D. R., et al. 2009, ApJS, 183, 261

De Robertis, M. M., Dufour, R. J., & Hunt, R. W. 1987, J. R. Astron. Soc. Canada, 81, 195

Henney, W. J., García-Díaz, M. T., O'Dell, C. R., & Rubin, R. H. 2013, MNRAS, 428, 691

Meaburn, J., López, J. A., Gutiérrez, L., et al. 2003, Rev. Mex. Astron. Astrofis., 39, 185

O'Dell, C. R., & Harris, J. A. 2010, AJ, 140, 985

O'dell, C. R., & Wen, Z. 1994, ApJ, 436, 194

Robberto, M., Soderblom, D. R., Bergeron, E., et al. 2013, ApJS, 207, 10

Shaw, R. A., & Dufour, R. J. 1995, PASP, 107, 896

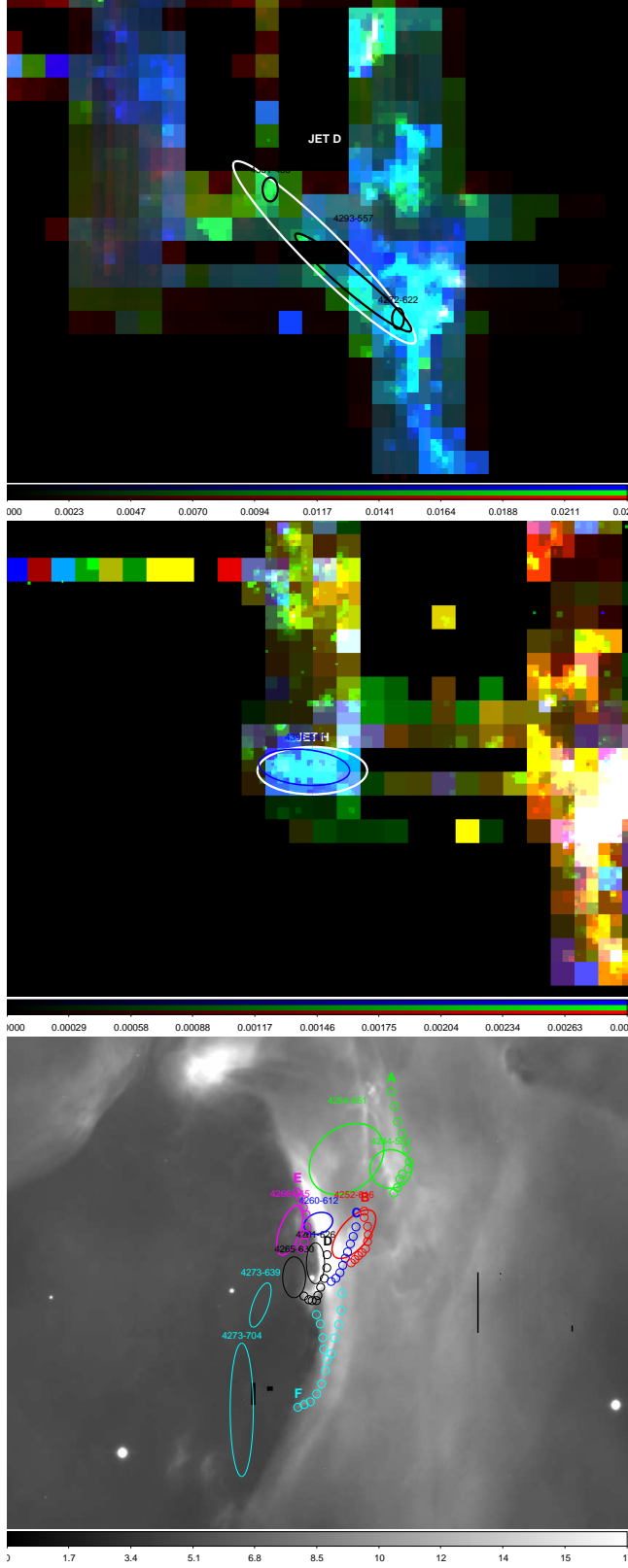Weilbacher, P. M., Monreal-Ibero, A., Kollatschny, W., et al. 2015, A&A, 582, A114

Figure 10. Figura provisional para que se entienda el texto. Arriba y medio los jets, abajo los arcos. Pensar cómo hacerla bonita.